A plasma source driven predator-prey like mechanism as a potential cause of spiraling intermittencies in linear plasma devices

D. Reiser,[1] N. Ohno,[2] H. Tanaka,[3] and L. Vela[4]
[1]*Institute for Energy and Climate Research - Plasma Physics, Research Center Jülich GmbH, Association FZJ-Euratom, D-52425 Jülich, Germany*
[2]*Department of Energy Engineering and Science, Graduate School of Engineering, Nagoya University, Furo-cho, Chikusa-ku, Nagoya 464-8603, Japan*
[3]*National Institute for Fusion Science, Toki 509-5292, Japan*
[4]*Physics Department, Universidad Carlos III de Madrid, Avda de la Universidad 30, 28911-Leganés, Madrid, Spain*

Three-dimensional global drift fluid simulations are carried out to analyze coherent plasma structures appearing in the NAGDIS-II linear device. The numerical simulations reproduce several features of the intermittent spiraling structures observed, for instance statistical properties, rotation frequency and the frequency of plasma expulsion. The detailed inspection of the three-dimensional plasma dynamics allows to identify the key mechanism behind the formation of these intermittent events. The resistive coupling between electron pressure and parallel electric field in the plasma source region gives rise to a predator-prey like dynamics where the axisymmetric mode represents the prey and the spiraling structure with low azimuthal mode number represents the predator. This interpretation is confirmed by a reduced one-dimensional quasilinear model derived on the basis of the findings in the full three-dimensional simulations. The reduced model can be used for quick analysis of parameter dependencies of the expulsion frequency and amplitudes. Results are presented on the variation of the predator-prey like process for different levels of plasma source strength and different plasma temperatures.

I. INTRODUCTION

Many linear plasma devices have been designed to explore the dynamics of coherent structures. Due to its similarities with intermittent events in the tokamak edge plasma it is expected that the detailed investigation of structure formation and blobby transport events in linear devices yield important insights into fusion relevant processes like Edge Localized Modes. Development of high-temporal-resolution measurements using fast-imaging cameras and Langmuir probes provided a wealth of information on plasma structures and their dynamics [1–5].

A particular feature often observed in several devices is the appearance of spiraling structures combined with irregular expulsion of plasma particles in the radial direction. Sometimes this effect appears for a particular operational regime only, i.e. for a suitable combination of magnetic field, plasma density and temperature. A detailed understanding of the underlying mechanism is still pending.

In this work we present three-dimensional numerical simulations for a linear configuration representing the conditions in the NAGDIS-II device [1; 2]. It is shown that our computational setup leads to simulation results resembling to a large extent the experimental results. A detailed comparison is presented based on the same techniques used previously for the statistical analysis of the experimental results. To gain more insight into the nature of the intermittencies observed we take advantage of the wealth of numerical data available and identify the most dominant driving mechanism. It is found that an imbalance of the electron pressure gradient and the parallel electric field in the plasma source region is the origin of the coherent structures observed. For a particular range of parameters the plasma dynamics shows a predator-prey like oscillation for a small number of azimuthal modes. In a subsequent step this finding is used to derive a reduced one-dimensional model. By comparison with the full three-dimensional simulations it is shown that this simplified model still contains basic ingredients of the intermittent transport. Additionally, its simple structure allows to perform easily a large number of parameter scans without extensive simulation runs. Conclusions are drawn on the intermittent expulsion frequency as a function of source strength and electron temperature. In a further step the results of the reduced model are used to derive an even more simplified zero-dimensional model to identify a class of plasma states which can be described by a Lotka-Volterra cycle.

The working hypothesis that the system tends to a state with minimized rate of change due to parallel force imbalances while maximizing the radial particle flow due to azimuthal perturbations provides a simple explanation for the key mechanism causing the appearance of spiraling intermittencies.

II. THREE-DIMENSIONAL GLOBAL DRIFT FLUID DYNAMICS IN CYLINDRICAL GEOMETRY

The numerical simulations in this work are based on the electrostatic drift-fluid model derived in detail in Ref. [6]. The equations for continuity, parallel momentum and electron temperature (see. Eqs. 11-15 in Ref. [6]) to describe the temporal evolution of the global profiles of particle density n, parallel electron velocity $v_\parallel$, parallel

ion velocity $u_\parallel$ and electron temperature T_e read

$$\frac{\partial n}{\partial t} + \mathbf{v}\cdot\boldsymbol{\nabla} n = -n\,\boldsymbol{\nabla}\cdot\mathbf{v} + S_n^e \tag{1}$$

$$\begin{aligned}\frac{\partial v_\parallel}{\partial t} + \mathbf{v}\cdot\boldsymbol{\nabla} v_\parallel = &-\frac{\nabla_\parallel p_e}{m_e n} + \frac{e\,\eta_\parallel}{m_e}\,J_\parallel - \frac{\alpha}{m_e}\,\nabla_\parallel T_e \\ &+\frac{e}{m_e}\,\nabla_\parallel\phi - \frac{S_n^e}{n}\,v_\parallel + \frac{S_\parallel^e}{m_e n}\end{aligned} \tag{2}$$

$$\begin{aligned}\frac{\partial u_\parallel}{\partial t} + \mathbf{u}\cdot\boldsymbol{\nabla} u_\parallel = &-\frac{e\,\eta_\parallel}{m_i}\,J_\parallel + \frac{\alpha}{m_i}\,\nabla_\parallel T_e \\ &-\frac{e}{m_i}\,\nabla_\parallel\phi - \frac{S_n^i}{n}\,u_\parallel + \frac{S_\parallel^i}{m_i n}\end{aligned} \tag{3}$$

$$\begin{aligned}\frac{\partial T_e}{\partial t} + \mathbf{v}\cdot\boldsymbol{\nabla} T_e = &-\frac{2}{3\,n}\,\boldsymbol{\nabla}\cdot\mathbf{q}_e - \frac{2}{3}\,T_e\,\boldsymbol{\nabla}\cdot\mathbf{v} \\ &-\frac{2}{3}\,\alpha\,\frac{J_\parallel}{e\,n}\,\nabla_\parallel T_e + \frac{2}{3}\,\frac{\eta_\parallel}{n}\,J_\parallel^2 - \frac{2}{3}\,\frac{\mathbf{S}_m^e\cdot\mathbf{v}}{n} \\ &+\frac{2}{3}\,\frac{S_n^e}{n}\left(\frac{1}{2}\,m_e\,v^2 - \frac{3}{2}\,T_e\right) + \frac{2}{3}\,\frac{S_E}{n}\end{aligned} \tag{4}$$

where $\mathbf{q}_e$ is the electron heat flux

$$\mathbf{q}_e = -\alpha\,T_e\,\mathbf{J}_\parallel/e - \kappa_\parallel^e\,\boldsymbol{\nabla}_\parallel T_e - \kappa_\perp^e\,\boldsymbol{\nabla}_\perp T_e \tag{5}$$

and $p_e = nT_e$, $J_\parallel = n(u_\parallel - v_\parallel)$ and ϕ are the electron pressure, the parallel current density and the electric potential, respectively. The total velocity of electrons is denoted by $\mathbf{v}$ and that of the ions by $\mathbf{u}$. The classical resistivity is denoted by $\eta_\parallel$ and S_n^e, $S_\parallel^e$, S_n^i, $S_\parallel^i$, $\mathbf{S}_m^e$, S_E are sources for particles, momentum and energy. The thermal force coefficient is set to $\alpha = 0.71$ and the quantities e, m_i and m_e have their standard meaning. The perpendicular velocities $\mathbf{v}_\perp$ and $\mathbf{u}_\perp$ of electrons and ions, respectively, are written in Helmholtz decomposition

$$\mathbf{v}_\perp = \mathbf{e}_z \times \boldsymbol{\nabla}_\perp \frac{\phi}{B} \equiv \mathbf{V}_E \tag{6}$$

$$\mathbf{u}_\perp = \boldsymbol{\nabla}_\perp\chi + \mathbf{e}_z \times \boldsymbol{\nabla}_\perp\psi + \mathbf{e}_z \times \boldsymbol{\nabla}_\perp \frac{\phi}{B} \tag{7}$$

where χ and ψ are potential fields describing the ion polarization drift. The covariant basis vector $\mathbf{e}_z$ is parallel to the homogeneous magnetic field $\mathbf{B} = B\,\mathbf{e}_z$ in the linear device with assumed cylinder symmetry. The velocities $\mathbf{v}_\perp$ and $\mathbf{u}_\perp$ can be determined by the following equations

$$\nabla_\perp^2\chi = -\frac{\nabla_\parallel J_\parallel}{en} \tag{8}$$

$$\nabla_\perp^2\psi = -\mathbf{e}_z\cdot\boldsymbol{\nabla}_\perp\times\mathbf{w}_\perp \tag{9}$$

$$\frac{m_i}{eB^2}\,\frac{\partial\nabla_\perp^2\phi}{\partial t} = -\nabla_\perp^2\chi - \boldsymbol{\nabla}_\perp\cdot\mathbf{w}_\perp \tag{10}$$

where $\mathbf{w}_\perp$ is a velocity given by

$$\begin{aligned}\mathbf{w}_\perp = \frac{m_i}{eB^2}\,\Big(&\mathbf{u}_\parallel\cdot\boldsymbol{\nabla}\boldsymbol{\nabla}_\perp\phi + \mathbf{V}_E\cdot\boldsymbol{\nabla}\boldsymbol{\nabla}_\perp\phi + \nu_{in}\,\boldsymbol{\nabla}_\perp\phi \\ &-\mu_\perp\,\boldsymbol{\nabla}_\perp\nabla_\perp^2\phi - \mu_\parallel\,\boldsymbol{\nabla}_\perp\nabla_\parallel^2\phi + \frac{S_n^i}{n}\,\boldsymbol{\nabla}_\perp\phi\Big)\end{aligned} \tag{11}$$

The damping coefficient ν_{in} takes into account ion-neutral collisions in the ion momentum balance. The coefficients $\mu_\parallel$ and $\mu_\perp$ introduce an artificial viscosity and represent a subscale damping of ion momentum (similar viscous terms are used for the other quantities too). It is to be noted that the vorticity equation Eq. 10 is a modified version of the vorticity equation Eq. 19 of Ref. [6], where it is shown that its particular form is an inevitable ingredient to fulfill the energy conservation of the model properly. However, the simplification, i.e. the Boussinesq approximation, used to derive the vorticity equation Eq. 10 in this work introduces only small errors and is advantageous in view of numerical stability.

III. SIMULATIONS FOR NAGDIS-II CONDITIONS

The model equations Eqs. 1-3 and 10 are solved numerically in a 3D cylindrical domain with coordinate ranges $0 \le r \le R$, $0 \le \theta \le 2\pi$ and $0 \le z \le L$. The equations are discretized using a standard second-order finite difference approach and for time stepping the Karniadakis scheme [12] is employed. To take into account the polarization drift properly an iteration of Eqs. 8, 9 and 10 is needed for each time step to compute the velocity potentials. At the casing, that is for $r = R$, the electric potential ϕ is set to zero, assuming a grounded perfect conductor as wall material. For the other quantities n, $v_\parallel$, $u_\parallel$ and T_e a zero radial gradient is prescribed. At the targets, here at $z = 0$ and $z = L$, sheath boundary conditions are imposed [13; 14]. The parallel ion velocity is $u_\parallel$ is set to sound speed $c_s = \sqrt{T_e/m_i}$ and for the density n and electron temperature T_e the gradient is set to zero allowing free convective outflow of particles and heat. The parallel current density $J_\parallel$ at the sheath entrance is determined by an electric potential arising due to charge accumulation at the target

$$J_\parallel = \pm enc_s\left[1 - \sqrt{\frac{m_i}{2\pi m_e}}\,\exp\left(-\frac{e\phi - e\phi_*}{T_e}\right)\right] \tag{12}$$

where ϕ_* is the electric potential at the targets which is assuemd to be constant. The "+ sign" refers to the target at $z = L$ and the "− sign" for the boundary at $z = 0$. The electric potential at the targets is determined by a zero gradient boundary condition. The particle sources for

electrons and ions are set equal and are described by

$$S_n^e = S_0 \exp\left[-\frac{4\,(z-L/4)^2}{(L/6)^2}\right] \times \times \frac{\tanh\left[a\,(r+r_0)\right] - \tanh\left[a\,(r-r_0)\right]}{2} \tag{13}$$

The shaping parameter a allows a continous transition between steep and smooth profiles. Its impact on the intermittent dynamics is studied in Ref. [7]. To come as close as possible to a reasonable simulation for a Helium-discharge in the NAGDIS-II device the following parameters are chosen: $m_i = 4\ m_p$, $B = 0.1$ T, $R = 10$ cm, $L = 2$ m, $a = 32.8\ \mathrm{m}^{-1}$, $r_0 = R/4$ and $S_0 = 10^{22}\ \mathrm{m}^{-3}\,\mathrm{s}^{-1}$. For the damping parameters we set $\mu_\perp = 0.15\ \mathrm{m}^2/\mathrm{s}$ and $\mu_\parallel = 5\ \mathrm{m}^2/\mathrm{s}$. A 32×32×32 computational grid in (r, θ, z) coordinates and a time step of $\Delta t = 4.2{\cdot}10^{-9}$ s is used. The simulation starts with an empty device and is running until a statistically stationary state is reached and the computational volume is filled with plasma.

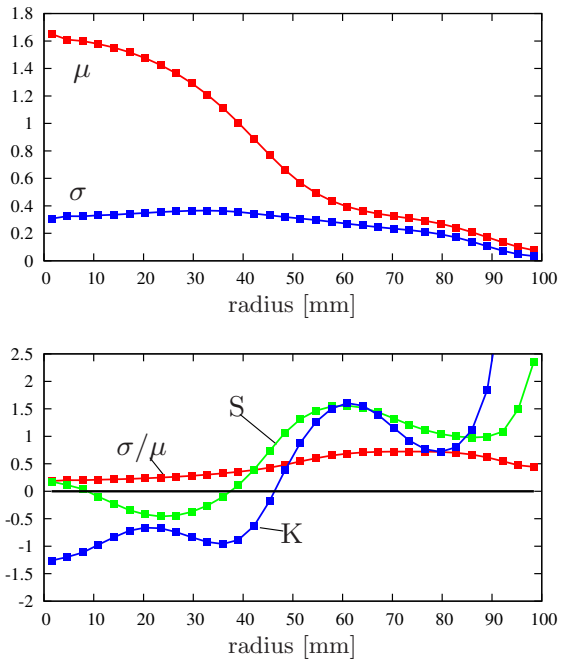

FIG. 1 (Color online) Radial profiles of the central moments of density fluctuationsin numerical simulations. Top: mean value μ and standard deviation σ in units of $10^{19}\mathrm{m}^{-3}$. Bottom: ratio σ/μ, skewness S and kurtosis K.

A. Numerical results and comparison with experiment

In this section it is demonstrated that the 3D-drift-fluid model employed is suitable to reproduce spiraling intermittent particle motion as observed in the linear device NAGDIS-II. This is done by comparing the saturated state of the numerical simulations with results reported

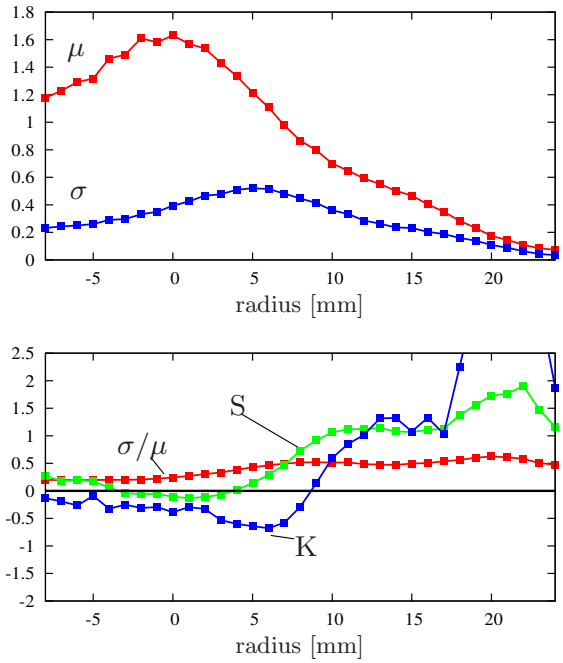

FIG. 2 (Color online) Radial profiles of the central moments of I_{sat} fluctuations in NAGDIS-II experiments. Top: mean value μ and standard deviation σ in units of 10^{-2}A. Bottom: ratio σ/μ, skewness S and kurtosis K.

on the statistics of 2D coherent structures in Refs. [1; 2]. The saturated state of the simulated plasma column is analyzed on the basis of a series of 3000 snapshots taken with an interval of 6.68 μs in the (r, θ)-planes at $z = 0$, $L/4$, $L/2$, $3L/4$, L. For the purpose of comparison with results obtained at the NAGDIS-II experiment we extracted the radial profiles of the first four central moments of the plasma density at $z = L/4$. The results for the mean value μ, the standard deviation σ, the skewness S and the kurtosis K are shown in Fig. 1. This figure qualitatively resembles to a large extent the experimentally found profiles of Fig. 2. There the radial profiles of the central moments of the ion saturation current $I_{\mathrm{sat}} \sim nT_e^{1/2}$ are shown which have been measured using a 4-pin Langmuir at the mid port of the NAGDIS-II device. Details of the experimental setup are described in Ref. [1]. It is important to note that the peak of the mean value of the ion saturation current, representing the electron density, is not located exactly at the center of the plasma column. Actually, it is shifted outward from the center of plasma column by 3-5 mm, probably due to some perturbations caused by the insertion of the Langmuir probe. Therefore, the exact center of the plasma column is located between -5 to -3 mm in Fig. 2. However, even if the actual radius of the plasma column in the simulation and the experiment is different, several qualitative features agree quite well. The different radial dimensions used in the numerical simulation result from the need to keep the computational time acceptable which increases with resolution. Nevertheless, in particu-

lar the pronounced non-Gaussian plasma fluctuations in the outer radial region is reproduced, where $S \gg 0$ and $K \gg 0$ (Gaussian statistics gives $S = 0$ and $K = 0$)., indicating intermittencies. In the inner region the plasma fluctuations seem to be closer to Gaussian, a result also in agreement with experiment. Additionally, in Fig. 3, a series of 2D plasma density snapshots taken at $z = L/4$ is shown. Again the results resemble strongly the experimental findings where similar spiraling intermittencies are observed (see Fig. 1a in Ref. [2]). The plasma column is rotating with a frequency of 3.2 kHz (experiment: 3.4 kHz) and the particles are expelled via irregular tails with a frequency of approximately 2.0 kHz (experiment: 3.2 kHz). Despite of these remarkable similarities, it is to be noted that the direction of azimuthal rotation in the simulations is opposite to the experimental observations. This is caused by the time averaged radial profile of the electric potential which is hollow in the experiment and determined by the PIG (Penning Ionization Gauge) discharge configuration. In the numerical simulation the profile is determined by the sheath boundary conditions giving a maximum of the electric potential in the center of the plasma column. Nevertheless, the similarities of the particle dynamics allows to conclude that a robust and dominant effect of the experiment is captured by the numerical model. To get more insight into the

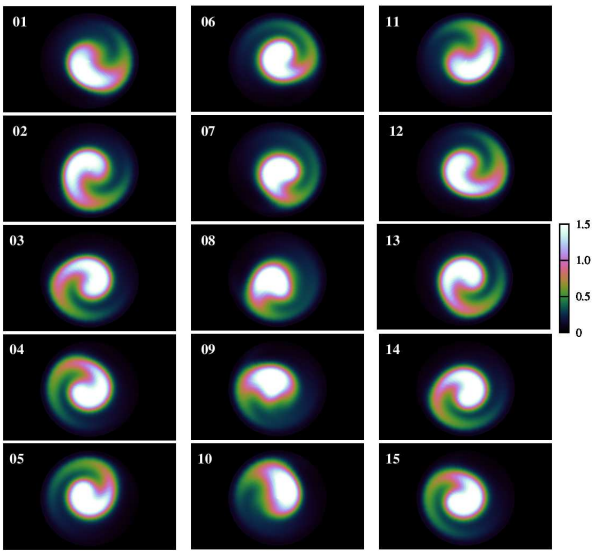

FIG. 3 (Color online) Snapshots of particle density in the r-θ-plane at $z = L/4$. The interval between two consecutive snapshots is 53.4 μs. The color coding gives the density in units of $10^{19}\mathrm{m}^{-3}$. The patterns are in good agreement with Fig. 1 (a) in Ref. [2].

structure of the intermittent dynamics a POD analysis (Proper Orthogonal Decomposition) is carried out similar to the analysis made previously using experimental data (see Ref. [1] for details of the method). The total series of 3000 snapshots is used for the POD to extract the spatial basis functions the time dependent dynamics consists of. The first 10 most dominant (normalized) base functions are shown in Fig. 4. The top figure of Fig. 5 proves that indeed the first 10 base modes are the most important contributors to the time dependent dynamics. It is obvious that the dominant contributions come from base modes with azimuthal mode number $m = 0$ and $m = 1$. Base modes with different symmetry, i.e. higher azimuthal numbers are only less pronounced. Considering the time traces of the first three base modes dominating the dynamics according to Fig. 5 top, one can find from Fig. 5 bottom a quasi-periodic temporal behaviour. Additionally, the overall behaviour of the modes with $m = 0$ and $m = 1$ symmetry is examined by considering averaged amplitudes defined as

$$E_m = \int_0^R |n_m|^2 \, r \, dr, \quad n_m = \frac{1}{2\pi} \int_0^{2\pi} n \, e^{-i\,m\,\theta} \, d\theta \tag{14}$$

The Fig. 6 shows the time traces of E_0, E_1 and E_2. Again this proves the importance of the $m = 0, 1$ modes. But also it can be seen that the overall dynamics is much more fitted in a clear periodic process. It is to be noted

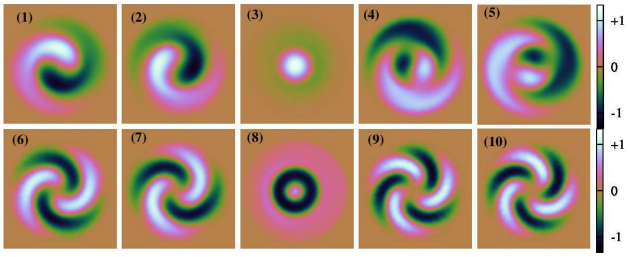

FIG. 4 (Color online) Base modes of the time series of density snapshots found by POD. The color coding is given in [a.u.].

that the phase relation between E_0 and E_1 resembles to a large extent the well-known predator-prey dynamics in biological models. This will be discussed more in detail in subsequent sections where it is shown that the predator-prey type of dynamics results from particular features of an asymptotic plasma state relevant for the plasma regime considered here. The temporal evolution of coherent structures, their statistics and quasi-oscillatory behaviour is very similar at the different z-locations considered in the numerical analysis. But it is found that the patterns observed appear first in the source region and with a certain delay at the other z-locations. The Fig. 7 shows the time traces of the strongest axisymmetric POD base mode (No. 3 in Figs. 4 and 5) at different parallel locations, i.e. in the source region at $z = L/4$ and three different points located in a distance $\pm L/4$ and $L/2$, respectively, away from the source region. It can be seen that the quasi-oscillatory dynamics in the source region is always ahead of the other locations. From this result it can be concluded that the spiraling events are originated close to the source region and the resulting structures are travelling quickly along the magnetic field lines to the targets as it is depicted in Fig. 8.

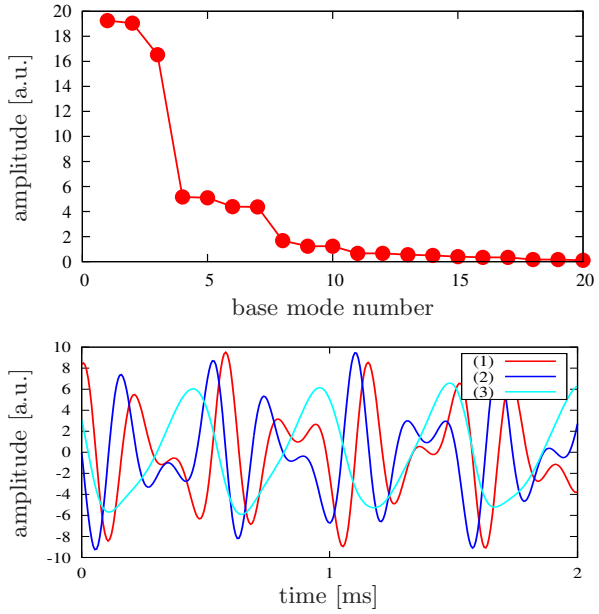

FIG. 5 (Color online) Top: POD base mode amplitudes vs mode number. Bottom: time traces of the base mode amplitudes for the three dominant modes.

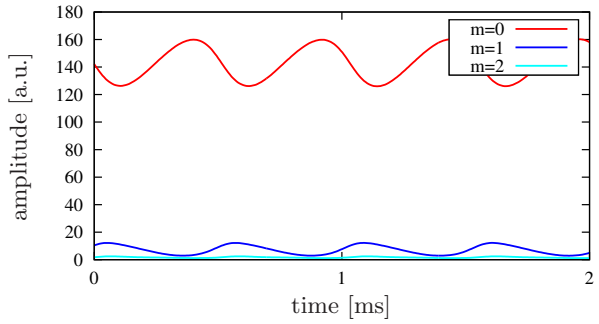

FIG. 6 (Color online) Time traces of the averaged amplitudes E_0 (red), E_1 (blue) and E_2 (cyan).

B. Model reduction

Now the numerical simulations allow to inspect in detail the relevance and magnitude of the different mechanisms interacting in the underlying model. It is found that the particular simulations for NAGDIS-II like parameters presented here can be described quite accurately by the reduced model

$$\frac{\partial n}{\partial t} + \mathbf{V}_E \cdot \boldsymbol{\nabla} n = -\nabla_\parallel \left(n\, v_\parallel \right) + \mu_\perp \nabla_\perp^2 n + S_n^e \tag{15}$$

$$\eta_\parallel J_\parallel = \frac{T_e \nabla_\parallel n}{e\, n} - \nabla_\parallel \phi \tag{16}$$

$$\frac{m_i}{eB^2} \left(\frac{\partial \nabla_\perp^2 \phi}{\partial t} + \mathbf{V}_E \cdot \boldsymbol{\nabla} \nabla_\perp^2 \phi \right) = \frac{\nabla_\parallel J_\parallel}{en} \tag{17}$$

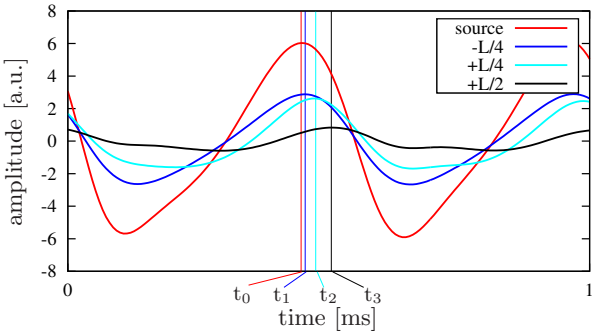

FIG. 7 (Color online) Time traces of amplitudes of the most dominant axisymmetric POD base mode. The positions of their maximum are marked by vertical lines at t_0, t_1, t_2 and t_3, where t_1-t_0=8 μs, t_2-t_0=28 μs and t_3-t_0=58 μs.

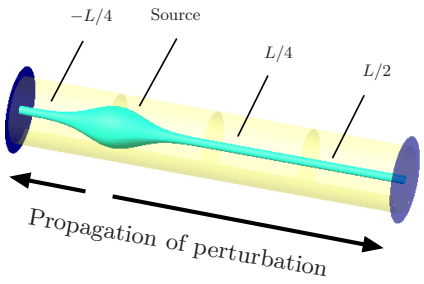

FIG. 8 (Color online) Coherent structures propagate along the magnetic field and are originated in the source region.

which is a true subset of the model Eqs. 1-3 and 10. Here $\mathbf{V}_E$ denotes the $E\times B$-velocity

$$\mathbf{V}_E = \frac{\mathbf{e}_z \times \boldsymbol{\nabla}_\perp \phi}{B} \tag{18}$$

The reduced model is confirmed by successive reduction of the numerical model. All terms neglected in the reduction from the full model have been proven to have little or no effect on the numerical results. Therefore, it can be concluded that – at least for this parameter range – electron inertia and parallel ion motion are less relevant for the development of the structures considered in this work.

C. Summary of findings in three-dimensional simulations

The three-dimensional simulations conducted for parameters close to the NAGDIS-II setup are able to reproduce several features of the plasma dynamics observed in the experiments. spiraling intermittent events lead to radial particle expulsion on time scales similar to the experiment. The POD and Fourier analysis prove that the 2D structures perpendicular to the magnetic field are dominated by patterns with low azimuthal mode numbers. The observed non-Gaussian statistics is similar to the NAGDIS-II results as well. Additionally, the careful inspection of time traces of the numerical data allows

the conclusion that the coherent structures are evolving close to the plasma source region and travel along the magnetic field. Moreover, the quasi-periodic behaviour of the averaged Fourier amplitides indicates a predator-prey like dynamics. A first hint on the basic mechanisms underlying the evolution and propagation of the coherent structures is provided by a reduced model confirmed by numerical experiments. The following analysis is devoted to an intepretation of these findings in terms of this reduced model.

IV. A QUASILINEAR PREDATOR-PREY LIKE MODEL

In this section the reduced model equations Eqs. 15-18 are used to derive an even more simplified framework to analyze the interaction between the axisymmetric $m=0$ mode and a single mode with $m\neq 0$ and to get more insight into the basic mechanisms leading to the spiraling intermittencies observed. A one-dimensional quasilinear model is substantiated and it is shown that basic features of the 3D dynamics presented in the previous section are reproduced qualitatively. For the purpose of simplification it is assumed that the temperature T_e is constant, i.e. $\eta_\parallel$ is constant too. The term $\sim \nabla_\parallel J_\parallel$ in the vorticity equation Eq. 17 is approximated by the use of Eq. 16 and a Hasegawa-Wakatani like approximation [8; 9]

$$\frac{\nabla_\parallel J_\parallel}{e\,n} = \frac{1}{e\,n_0\,\eta_\parallel}\left(\frac{\phi}{L_\phi^2} - \frac{T_e\,n}{e\,n_0\,L_n^2}\right) \tag{19}$$

where n_0 denotes the symmetrical angle averaged piece of the density

$$n = n_0 + \widetilde{n} \quad ; \quad n_0 = \langle n\rangle \equiv \frac{1}{2\pi}\int_0^{2\pi} n\,d\theta \tag{20}$$

and $\widetilde{n}$ contains the non-symmetric piece. The parallel derivative of the parallel electron flow $nv_\parallel$ in Eq. 15 is estimated by

$$\nabla_\parallel\left(n\,v_\parallel\right) = \frac{n\,v_0}{L_v} \tag{21}$$

with a constant velocity v_0. Additionally neglecting the dissipative terms in the vorticity equation the model Eqs. 15-17 becomes

$$\frac{\partial n}{\partial t} + \mathbf{V}_E\cdot\boldsymbol{\nabla} n = -\frac{n\,v_0}{L_v} + \mu_\perp\,\nabla_\perp^2 n + S_n^e \tag{22}$$

$$\frac{\partial \nabla_\perp^2\phi}{\partial t} + \mathbf{V}_E\cdot\boldsymbol{\nabla}\nabla_\perp^2\phi = \frac{B^2}{m_i\,n_0\,\eta_\parallel}\left(\frac{\phi}{L_\phi^2} - \frac{T_e\,n}{e\,n_0\,L_n^2}\right) \tag{23}$$

Now it is assumed that the the non-symmetric pieces of n and ϕ are consisting of a single azimuthal mode with mode number m (for the results of Sec. III it would be $m=1$)

$$n = n_0(r,t) + n_m(r,t)\,e^{im\theta} + n_m^*(r,t)\,e^{-im\theta} \tag{24}$$

$$\phi = \phi_0(r,t) + \phi_m(r,t)\,e^{im\theta} + \phi_m^*(r,t)\,e^{-im\theta} \tag{25}$$

Then the following quasilinear equations result

$$\begin{aligned}\frac{\partial n_0}{\partial t} &= \frac{2\,m}{rB}\,\frac{\partial}{\partial r}\left(\mathrm{Im}\left\{n_m\,\phi_m^*\right\}\right) - \frac{n_0\,v_0}{L_v}\\ &\quad +\mu_\perp\left(\frac{\partial^2 n_0}{\partial r^2} + \frac{1}{r}\,\frac{\partial n_0}{\partial r}\right) + S_n^e\end{aligned} \tag{26}$$

$$\begin{aligned}\frac{\partial n_m}{\partial t} &= \frac{i\,m}{rB}\,\frac{\partial n_0}{\partial r}\,\phi_m - \frac{i\,m}{rB}\,\frac{\partial \phi_0}{\partial r}\,n_m - \frac{n_m\,v_0}{L_v}\\ &\quad +\mu_\perp\left(\frac{\partial^2 n_m}{\partial r^2} + \frac{1}{r}\,\frac{\partial n_m}{\partial r} - \frac{m^2}{r^2}\,n_m\right)\end{aligned} \tag{27}$$

$$\frac{\partial w_0}{\partial t} = \frac{2\,m}{rB}\,\frac{\partial}{\partial r}\left(\mathrm{Im}\left\{w_m\,\phi_m^*\right\}\right) + C_\phi\,\phi_0 - C_n \tag{28}$$

$$\frac{\partial w_m}{\partial t} = \frac{i\,m}{rB}\,\frac{\partial w_0}{\partial r}\,\phi_m - \frac{i\,m}{rB}\,\frac{\partial \phi_0}{\partial r}\,w_m + C_\phi\,\phi_m - C_n\,\frac{n_m}{n_0} \tag{29}$$

where the functions C_ϕ and C_n represent the Wakatani term Eq. 19

$$C_\phi = \frac{B^2}{m_i\,n_0\,\eta_\parallel\,L_\phi^2}, \quad C_n = \frac{B^2\,T_e}{e\,m_i\,n_0\,\eta_\parallel\,L_n^2} \tag{30}$$

and the transformed Laplacians of the electric potential read

$$w_0 = \frac{\partial^2\phi_0}{\partial r^2} + \frac{1}{r}\,\frac{\partial\phi_0}{\partial r} \tag{31}$$

$$w_m = \frac{\partial^2\phi_m}{\partial r^2} + \frac{1}{r}\,\frac{\partial\phi_m}{\partial r} - \frac{m^2}{r^2}\,\phi_m \tag{32}$$

A. Numerical studies on quasilinear dynamics in the source region

The set of 1D equations Eqs. 26-29 can be solved easily by half-analytical methods. It describes the evolution of density and electric potential in an (r,θ)-plane with parallel dynamics prescribed by the parameters v_0, L_v, L_n and L_ϕ. In the following these equations are solved for a range of parameters close to the source region in the 3D simulations presented above. For this purpose the model parameters are chosen as: $m_i = 4$ m$_p$, $B = 0.1$ T, $R = 10$ cm, $T_e = 3$ eV, $m = 1$, $L_n = 0.8$ m, $L_n^2/L_\phi^2 = 0.4$,

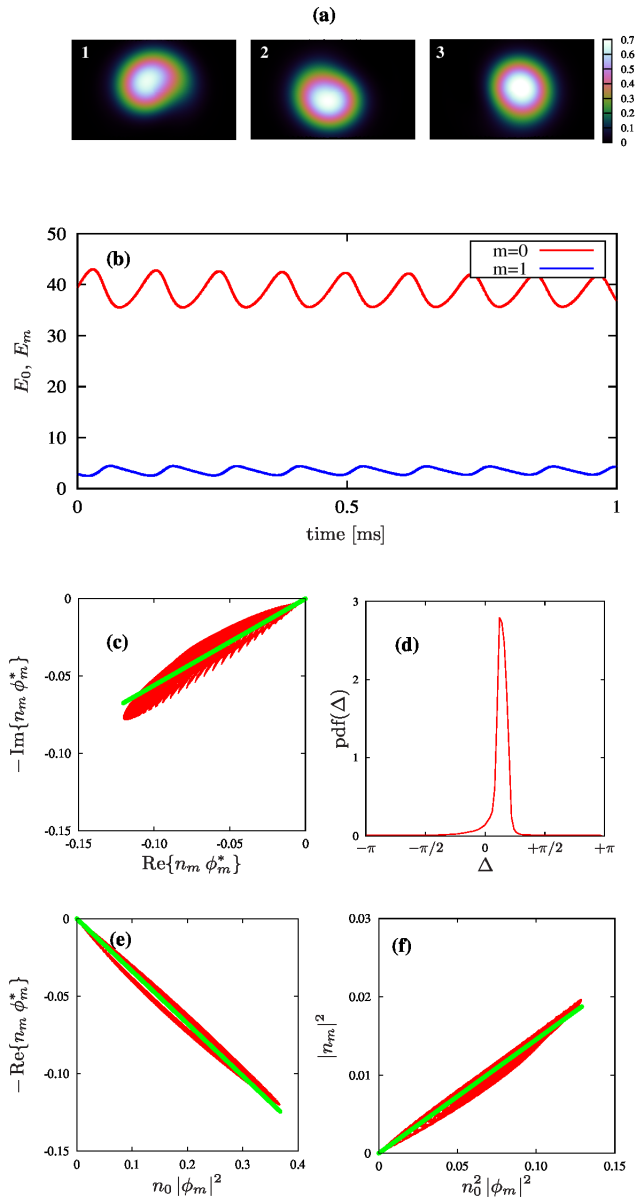

FIG. 9 (Color online) (a) Three snapshots taken with 21 μs interval. (b) Time traces of averaged amplitudes E_0 and E_1. (c) Scatter plot of $-\,\mathrm{Im}\{n_m\,\phi_m^*\}$ vs $\mathrm{Re}\{n_m\,\phi_m^*\}$. (d) pdf of phase shift Δ. (e) Scatter plot of $-\,\mathrm{Re}\{n_m\,\phi_m^*\}$ vs $n_0\,|\phi_m|^2$. (f) Scatter plot of $|n_m|^2$ vs $n_0^2\,|\phi_m|^2$. The slope k of the fit curves (green) is $k=0.56$, -0.34, 0.145 for Figs. c,e,f, respectively.

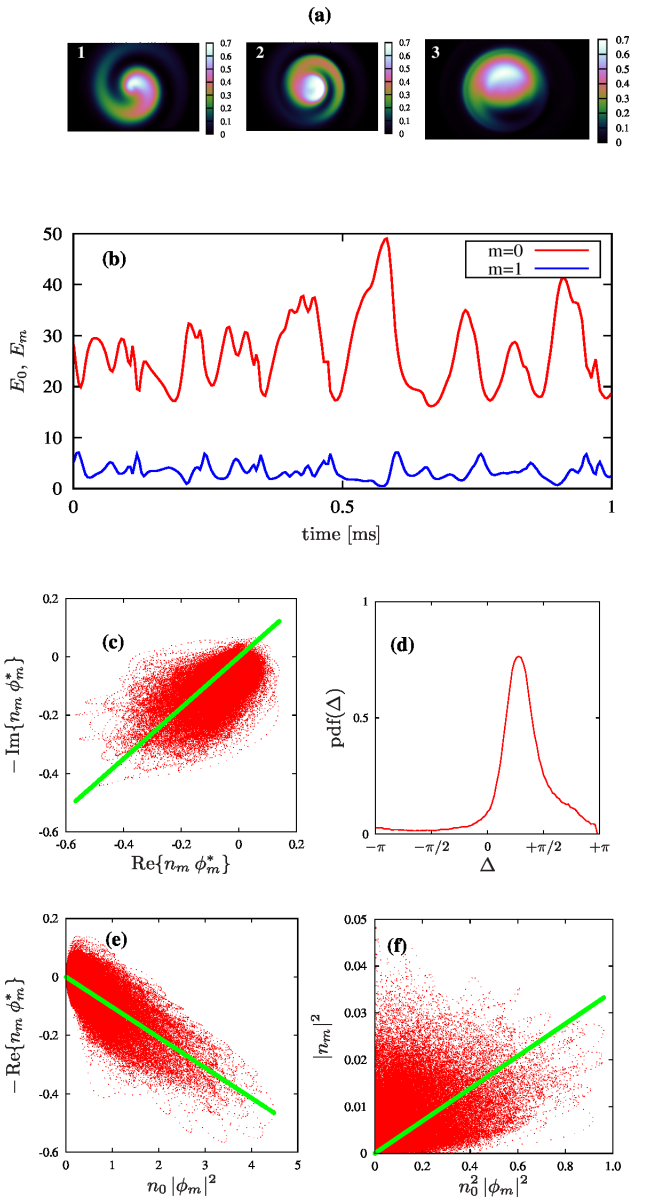

FIG. 10 (Color online) Numerical results analogous to Fig. 9, but obtained for ratio L_n^2/L_ϕ^2 reduced 0.1 in the simulation. The slope k of the fit curves (green) is $k=0.877$, -0.37, 0.035 for Figs. c,e,f, respectively.

For the damping parameter we use $\mu_\perp = 0.5$ m^2/s and the source profile is prescribed by

$$S_n^e = S_0\,\frac{\tanh\left[a\,(r+r_0)\right] - \tanh\left[a\,(r-r_0)\right]}{2} \qquad (33)$$

with source strength S_0=4.8·10^{23} m^{-3} s^{-1}, $r_0 = R/4$ and shaping parameter $a = 56.5$ m^{-1}. Finally the parallel flow term is prescribed by $v_0/L_v = 4.8{\cdot}10^4$ s^{-1}. Of course the reduction to a 1D model introduces uncertainties in the choice of several new parameters. The values used here are estimates to obtain a reasonable match to the conditions in the source region of the 3D simulations presented in the previous sections. Results of 1D computations based on this choice are presented in Fig. 9 and Fig. 10. In the top row three snapshots of plasma density are shown. The patterns of Fig. 10a are similar to the structures shown in Fig. 3, whereas the snapshots of Fig. 9a show an excentrically rotating plasma column. On the other hand the Fig. 9b shows time traces of E_0 and E_m in good qualitative agreement with the results of Fig. 6, even though the period of the predator-prey cycle is different. Contrary to this the time traces of Fig. 10b are less periodic and show an intermittent behaviour.

These two examples are typical results for the 1D model and most of the numerical tests done give results somewhere in between a relatively quiet plasma rotation and intermittent dynamics. Also, it is important to emphasize that the numerical results of the quasilinear model are very sensititve to the choice of input parameters, i.e. source strength, gradient length, source shape etc. Their quantitative significance is therefore limited. However, it can be concluded that basic qualitative properties of the 3D model are still contained in the strongly simplified quasilinear model derived in this section and this allows to draw conclusions about the underlying mechanisms. For this purpose the analysis is extended by additional findings presented in the Figs. 9c-9f and Figs. 10c-10f. The Figs. 9c and 10c show scatter plots of $\mathrm{Im}\{n_m\,\phi_m^*\}$ vs $\mathrm{Re}\{n_m\,\phi_m^*\}$ for each radial position $0<r<R$ and for 3000 time points. The Figs. 9e and 10e show the scatter plots of $\mathrm{Re}\{n_m\,\phi_m^*\}$ vs $n_0\,|\phi_m|^2$ and in Figs. 9f and 10f the results for $|n_m|^2$ vs $n_0^2\,|\phi_m|^2$ are plotted. The meaning of these quantities becomes clear when we recall that in the quasilinear model the averaged radial particle flux Γ_r due to the non-symmetric pieces $\widetilde{n}$ and $\widetilde{\phi}$ is given by

$$\Gamma_r = -\left\langle \frac{\widetilde{n}}{rB}\,\frac{\partial\widetilde{\phi}}{\partial\theta}\right\rangle = -\frac{2m}{rB}\,\mathrm{Im}\,\{n_m\,\phi_m^*\} \tag{34}$$

and that the integral over the averaged rate of change of the non-symmetric piece of kinetic energy reads

$$\begin{aligned}\frac{1}{2}\int\left\langle\frac{\partial\widetilde{V}_E^2}{\partial t}\right\rangle r\,dr &= -2\int \mathrm{Re}\left\{\frac{\phi_m}{B^2}\,\frac{\partial w_m^*}{\partial t}\right\} r\,dr\\ &= 2\int\frac{m}{rB^3}\,\frac{\partial\phi_0}{\partial r}\,\mathrm{Im}\,\{\phi_m\,w_m^*\}\,r\,dr \\ &-2\int\left(\frac{C_\phi}{B^2}\,|\phi_m|^2-\frac{C_n}{n_0B^2}\,\mathrm{Re}\,\{n_m\,\phi_m^*\}\right) r\,dr\end{aligned} \tag{35}$$

Thus, the scatter plots provides an insight into the interplay of radial transport and the impact of parallel dynamics on the flow velocity. Notice that the Eq. 35 is valid only if ϕ_m is zero at r=0 and at the outer radial boundary, but actually this boundary condition is used in our 1D computations. First, we consider the results for the more quiet plasma with pronounced predator-prey cycles in Fig. 9. The scatter plots Figs. 9c, 9e and 9f show a clear linear dependence between the respective quantities. According to Eqs. 34 and 35 this provides a certain relation between the radial flux Γ_r and the rate of change of kinetic energy due to a parallel current density gradient. The green lines indicate a linear fit over all points plotted. It is remarkable that similar linear relations can be found in the analysis of the 3D simulation as well. The corresponding scatter plots are shown in Fig. 11a, 11c and 11d. The scatter plots of Figs. 9c, 10c and 11a contain the information on the phase shift between n_m and ϕ_m. This can be seen by rewriting n_m and ϕ_m in phasor form

$$n_m = |n_m|\,e^{i\vartheta},\quad \phi_m = |\phi_m|\,e^{i(\vartheta+\Delta)} \tag{36}$$

The phase shift is denoted by Δ and it follows

$$\mathrm{Im}\{n_m\,\phi_m^*\} = -\,\mathrm{Re}\{n_m\,\phi_m^*\}\,\tan\Delta \tag{37}$$

To support the analysis of the phase shift additionally

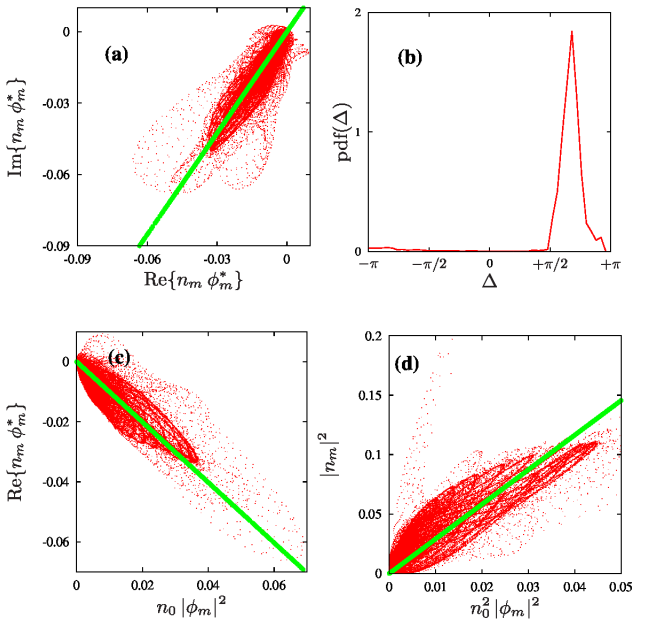

FIG. 11 (Color online) (a) Scatter plot of $\mathrm{Im}\{n_m\,\phi_m^*\}$ vs $\mathrm{Re}\{n_m\,\phi_m^*\}$. (b) pdf of phase shift Δ. (c) Scatter plot of $\mathrm{Re}\{n_m\,\phi_m^*\}$ vs $n_0\,|\phi_m|^2$. (d) Scatter plot of $|n_m|^2$ vs $n_0^2\,|\phi_m|^2$. The slope k of the fit curves (green) is $k=1.42$, -1.0, 2.91 for Figs. c,e,f, respectively.

the probability distribution function (pdf) of the phase shift Δ is shown in Figs. 9d, 10d and 11b. A strong peak occurs for $\Delta=0.16\,\pi$ in Fig. 9d, at $\Delta=0.23\,\pi$ in Fig. 10d and at $\Delta=0.70\,\pi$ in Fig. 11b, where in particular Fig. 9d indicates an almost constant phase shift everywhere. To interpret these results for the phase shift, we refer to the Figs. 9e and 11c. In both cases an approximate proportionality

$$\mathrm{Re}\{n_m\,\phi_m^*\} = k\,n_0\,|\phi_m|^2 \tag{38}$$

with constant k is found. This gives

$$|\phi_m| = \frac{\cos\Delta}{k\,n_0}\,|n_m| \tag{39}$$

and inserting this expression into Eq. 34 for the radial particle flux Γ_r leads to

$$\Gamma_r = \frac{m}{rB}\,\frac{\sin 2\Delta}{k\,n_0}\,|n_m|^2 \tag{40}$$

For $k>0$ (like in Figs. 9e) this is maximum for $\Delta=\pi/4$, whereas for $k<0$ (like in Fig. 11c) the maximum is at $\Delta=3\pi/4$. These values are quite close to the numerically obtained averaged phase shifts and it seems that the plasma tends to maximize the radial particle flux if

$\mathrm{Re}\{n_m\,\phi_m^*\}$ and $n_0\,|\phi_m|^2$ are constrained by a certain linear relation. Even for the less pronounced linear relation of Fig. 10e the value of the averaged phase shift taken from the pdf is very close to $\pi/4$. Now the fit procedure for the scatter plots in Fig. 9e and Fig. 10e give a poportionality $\mathrm{Re}\{n_m\,\phi_m^*\} \approx -k\,n_0\,|\phi_m|^2$, with $k = 0.34$ in Fig. 9e and $k = 0.37$ in Fig. 10e. According to the simulation parameters used ($C_\phi/C_n = 0.4$) this means that the relation

$$\mathrm{Re}\,\{n_m\,\phi_m^*\} = n_0\,\frac{C_\phi}{C_n}\,|\phi_m|^2 \tag{41}$$

is approximately fulfilled and consequently the integral in the third line of Eq. 35 is almost zero. So, in physical terms it can be concluded for the 1D model that the plasma state is characterized by a strong suppression of the rate of change of kinetic energy due to parallel current gradients. Of course for the broad distribution of points in Fig. 10e the suppression is fulfilled in a statistical sense only. Most of the points do not lie close to the fit curve. It is shown in the next section that fulfillment of Eq. 41 and an almost constant phase shift Δ are strongly related to the predator-prey signature in the interplay of E_0 and E_m in Fig. 9b and accordingly its absence in Fig. 10b. Of course the relation Eq. 41 is meaningful for the quasilinear model only. But, it is recalled that the Hasegawa-Wakatani like approximation in the quasilinear model implies the correspondence

$$\left\langle \frac{\phi\,\nabla_\parallel J_\parallel}{n\,m_i} \right\rangle \approx \frac{2C_\phi}{B^2}\,|\phi_m|^2 - \frac{2C_n}{n_0 B^2}\,\mathrm{Re}\,\{n_m\,\phi_m^*\} \tag{42}$$

Therefore, we extend the findings for the 1D model to the 3D case and presume that the strong correlation of $\mathrm{Re}\{n_m\,\phi_m^*\}$ and $n_0\,|\phi_m|^2$ in the 3D case is constrained by the tendency to suppress the parallel current drive for the $E\times B$ kinetic energy as well.

Finally, the scatter plots Fig. 9f, 10f and 11d are a cross check to support the findings and to make sure that the dependence on n_0 in the relations found is taken into account correctly. For this purpose the relation

$$|n_m|^2 = \frac{C_\phi^2}{C_n^2\,\cos^2\Delta}\,n_0^2\,|\phi_m|^2 \tag{43}$$

is considered which results from a combination of Eqs. 37 and 41. The fit in Fig. 9f provides $|n_m|^2 \approx 0.15\,n_0^2\,|\phi_m|^2$ which agrees with the previous results extracted here. The scatter plot of Fig. 10f does not show a clear functional relation at all and the points seem to be randomly scattered. Again we remark that this randomness and the loss of simple functional dependencies between the Fourier modes n_m and ϕ_m is strongly connected with the loss of predator-prey signature, or reversely, the predator-prey cycles like in Fig. 9b are always accompanied by tight relations like in Figs. 9c-9f. We conclude this section with examples of the qualitative changes with varying plasma parameters. The Fig. 12 shows spectra of the

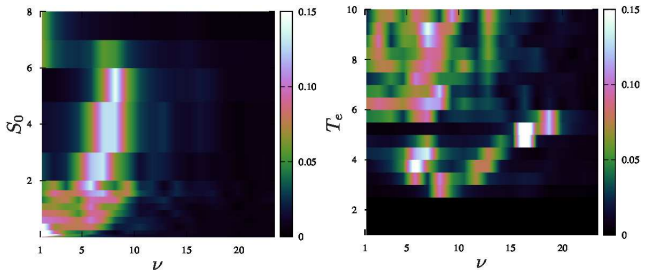

FIG. 12 (Color online) Spectra of E_m fluctuations for different source strengths S_0 (left figure) and electron temperature T_e. The source strength S_0 is given in units of $10^{23}\mathrm{m}^{-3}\mathrm{s}^{-1}$, the temperature T_e in units of eV and the frequency ν in kHz.

E_m fluctuations for parameter scans of electron temperature T_e and source strength S_0 in the 1D model simulations. Starting with the parameters used to perform the simulations illustrated by Fig. 9 the source strength is varied between $1.0{\cdot}10^{21}$ $\mathrm{m}^{-3}\mathrm{s}^{-1}$ and $8.0{\cdot}10^{23}$ $\mathrm{m}^{-3}\mathrm{s}^{-1}$ (Fig. 12 left). In a second scan only the temperature T_e is varied between 1 eV and 10 eV (Fig. 12 right). For a more convenient comparison the spectra are normalized such that the integral over the non-constant components of the density fluctuations is 1. In both spectra one can identify three types of spectra: (1) a region with zero fluctuations, (2) a region with a few pronounced peaks and (3) a region with relative broad spectrum of frequencies. The scan over S_0 shows that oscillations close to 9 kHz are present in the range between $2{\cdot}10^{23}$ $\mathrm{m}^{-3}\mathrm{s}^{-1}$ and $6{\cdot}10^{23}$ $\mathrm{m}^{-3}\mathrm{s}^{-1}$. This is the range where a pronounced predator-prey cycle dominates the plasma column. For values of S_0 below $2{\cdot}10^{23}$ $\mathrm{m}^{-3}\mathrm{s}^{-1}$ the spectrum becomes broad, which reflects an intermittent behaviour with bursty events instead of smooth cycles. Above $6{\cdot}10^{23}$ $\mathrm{m}^{-3}\mathrm{s}^{-1}$ the mode amplitude E_m is completely damped and no predator-prey cycle develops. Considering the T_e scan, the predator-prey range is between 3 and 5.5 eV which can be identified again by a few pronounced peaks in the spectrum. Below 3 eV no oscillation of n_m develops. But in this case this reflects a constant non-zero Fourier mode E_m leading to an excentric rotation of the plasma column. Above $T_E = 5$ eV the broad spectrum again reveals an intermittent plasma transport.

B. Predator-prey cycles and a conjectured asymptotic plasma state

To summarize, the results of 1D and 3D simulations led us to the working hypothesis that the predator-prey dynamics observed in the interplay of averaged Fourier modes E_0 and E_m is connected to a specific plasma state. This state can be characterized by a tendency to minimize the ploidally averaged rate of change in kinetic energy due to parallel current gradients and simultaneously maximizing the angle averaged radial particle flow due to

low-m modes, i.e.

$$\left\langle \left(\frac{\phi \, \nabla_\parallel J_\parallel}{n \, m_i} \right)^2 \right\rangle = \text{min!}, \quad - \left\langle \frac{\widetilde{n}}{rB} \, \frac{\partial \widetilde{\phi}}{\partial \theta} \right\rangle = \text{max!} \tag{44}$$

It is conjectured that for a certain range of plasma parameters a strong tendency towards this state governs the plasma dynamics and that intermittencies occur if other effects hinder the system to follow this trend. The particular link between the predator-prey cycles and the specific plasma state characterized by Eqs. 37 and 41 with a constant phase shift Δ is elucidated in the next section.

V. THE LIMIT CYCLE IN LOTKA-VOLTERRA APPROXIMATION

The results and the discussion of the previous section show that the particular predator-prey limiting cycle observed can be characterized by the tendency of the plasma modes to fulfill the relation

$$\text{Im}\left\{ n_m \, \phi_m^* \right\} = - \frac{C_n}{2 \, C_\phi} \, \frac{\sin 2\Delta}{n_0} \, |n_m|^2 \tag{45}$$

which is derived by inserting Eqs. 43 and 41 into Eq. 37. In this section it is shown that this asymptotic predator-prey interplay of the averaged mode amplitudes E_0 and E_m is closely related to a Lotka-Volterra system. To elucidate this we derive from Eqs. 14, 26 and 27 the evolution equations

$$\frac{\partial E_0}{\partial t} = - \frac{2m}{B} \int \text{Im}\left\{ n_m \, \phi_m^* \right\} \, \frac{\partial n_0}{\partial r} \, dr - \frac{v_0}{L_v} \, E_0 + \int S_n^e n_0 \, r \, dr \tag{46}$$

$$\frac{\partial E_m}{\partial t} = \frac{2m}{B} \int \text{Im}\left\{ n_m \, \phi_m^* \right\} \, \frac{\partial n_0}{\partial r} \, dr - \frac{2 \, v_0}{L_v} \, E_m \tag{47}$$

where viscous effects have been neglected and it is assumed that n_0 is vanishing at the outer radial boundary $r{=}R$ while having a zero gradient at $r{=}0$. Due to relation Eq. 45 one obtains for the interaction integral of Eqs. 46 and 47 the result

$$\int \text{Im}\left\{ n_m \, \phi_m^* \right\} \, \frac{\partial n_0}{\partial r} \, dr = - \int \frac{C_n \sin 2\Delta}{2 \, C_\phi} \, \frac{\partial n_0}{\partial r} \, \frac{|n_m|^2}{n_0} \, dr \tag{48}$$

In case that n_0 has a radial shape close to a Gaussian one can write

$$n_0 \approx \sqrt{\frac{2 \, E_0^2}{n_*^2 \, \rho_s^4}} \, \exp\left(- \frac{E_0 \, r^2}{2 \, n_*^2 \, \rho_s^4} \right) \tag{49}$$

where n_* is a constant scaling density and $\rho_s^2 = c_s^2 / \omega_i^2$, $c_s^2 = T_e / m_i$ and $\omega_i = eB/m_i$. This introduces a certain relation between the averaged amplitude E_0 and the axisymmetric density n_0. For large enough device radius $R \gg n_* \, \rho_s^2 / \sqrt{E_0}$ this gives

$$\int_0^R n_0^2 \, r \, dr \approx E_0 \tag{50}$$

and also a linear variation of the logarithmic derivative proportional to the intergal E_0 results

$$\frac{1}{n_0} \, \frac{\partial n_0}{\partial r} = - \frac{E_0 \, r}{n_*^2 \, \rho_s^4} \tag{51}$$

The Gaussian shape assumed in Eq. 49 is typical for experiments at NAGDIS-II. Moreover, it is found in the numerical simulations that $\bar{n}_0 \sim S_n^e$, i.e. the average symmetric density profile closely follows the source shape which has been chosen close to a Gaussian in this work. Therefore, Eqs. 46 and 47 can be approximated by

$$\frac{\partial E_0}{\partial t} = - \kappa \, E_m \, E_0 + \delta \, E_0 \tag{52}$$

$$\frac{\partial E_m}{\partial t} = \kappa \, E_m \, E_0 - \gamma \, E_m \tag{53}$$

with κ, δ and γ defined by

$$\kappa = \frac{m \, T_e \, L_\phi^2 \, \sin 2\Delta}{eB \, n_*^2 \, \rho_s^4 \, L_n^2}, \quad \delta = S - \frac{v_0}{L_v}, \quad \gamma = \frac{2 \, v_0}{L_v} \tag{54}$$

Here the constant parameter S represents the source strength. Thus, for constant parameters κ, δ and γ the temporal evolution of the averaged amplitudes E_0 and E_m is reasonably well approximated by the Lotka-Volterra system Eqs. 52 and 53. The classical Lotka-Volterra system is a well-known example of a predator-prey model and is widely studied in the literature (see Ref. [11] and references therein). According to the as-

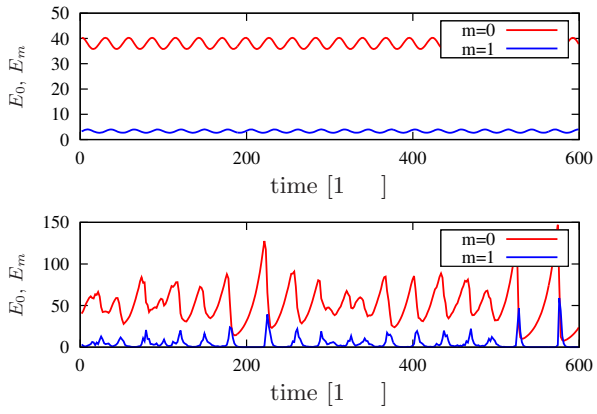

FIG. 13 (Color online) Time traces of E_0 and E_m obtained from the Lotka-Volterra model Eqs. 52 and 53. Top: for constant phase shift $\Delta = \pi/4$. Bottom: for a random phase shift Δ.

sumptions used to derive Eqs. 52 and 53, it can be concluded that the Lotka-Volterra cycle corresponds to the situation illustrated by Fig. 9, with peaked pdf(Δ) shown in Fig. 9d and prominent predator-prey cycles shown in Fig. 9b. But, if Δ is randomly distributed, which would correspond to Fig. 10d, the Eqs. 52 and 53 do not describe the classical Lotka-Volterra oscillations anymore. In this case the system becomes intermittent. This is illustrated by Fig. 13 where two numerical examples are compared for parameters $\kappa\, n_*^2\rho_s^2/\omega_i = 0.02$, $\delta/\omega_i = 0.066$ and $\gamma/\omega_i = 0.76$. Firstly, a constant phase shift $\Delta = \pi/4$ is used (Fig. 13 top). In the second example a randomly distributed phase shift $\Delta = (1 + 0.9\,\xi)\ \pi/4$ with ξ a uniformly distributed random number between 0 and 1 (Fig. 13 bottom). To mimic a certain correlation time of the variation of Δ the value of ξ is updated in intervals of $0.003\,T$ only, where $T = 6/\omega_i$ is the total time interval considered. The initial conditions for the time integration are $E_0 = 40$ and $E_m = 5$ given in units of $n_*^2\rho_s^2$. The Fig. 13 top shows the unperturbed Lotka-Volterra cycle for constant phase shift $\Delta = \pi/4$. The Fig. 13 bottom shows the result for the randomly distributed phase shift with correlation. Obviously an intermittent behaviour occurs similar to the results of Fig. 10 where a broad distribution of Δ is present. We consider this result as an additional evidence for the hypothesis that the unperturbed predator-prey state with almost fixed phase shift between n_m and ϕ_m can be regarded as an asymptotic "ideal" state. The plasma tends towards this state but certain hindrance might destabilize it. Therefore, if the perturbations are strong, it acts just as a weak attractor, and the distribution of the phase shift Δ becomes more broadened. This kind of broadening leads to a randomized coupling of E_0 and E_m and an intermittent dynamics results.

VI. SUMMARY AND CONCLUSIONS

In this work it is shown that 3D simulations based on a well established model of drift-fluid dynamics (Eqs. 1-3 and 10) reproduce many features of spiraling intermittent particle motion in the linear device NAGDIS-II [1; 2]. Despite certain discrepancies between theoretical and experimental results (direction of radial electric field, details of plasma source) broad qualitative agreement is found with respect to statistical properties (Fig. 1) and coherent structures (Fig. 3) of plasma density. A POD analysis performed for time traces of plasma density proves that the 2D patterns in the (r, θ)-plane are dominated by low-m modes, here $m = 1$ and $m = 2$, and that their amplitudes show a quasi-oscillatory time characteristic (Figs. 4-5). The time traces of radially averaged low-m Fourier amplitudes show an interplay resembling typical predator-prey mechanisms where the axisymmetric mode is the prey and the low-m modes are the predator (Fig. 6). The analysis of time shifts between different locations along the cylinder axis of the linear device proves that the particular dynamics observed originates close to the plasma source region (Figs. 7-8).

Besides this remarkable agreement between simulation results and experiment, additionally the 3D simulations allow to extract the model subset Eqs. 15-17 as main cause for the intermittent dynamics.

Based on these findings a further step is done in model reduction and a quasilinear 1D model Eqs. 26-29 is derived to gain more insight into the underlying physics in the source region. Its numerical exploration gives results similar to the 3D case (Figs. 9-11). Furthermore, the results indicate a strong correlation between the low-m Fourier modes of density n_m and electric potential ϕ_m, described by the relations Eqs. 37, 41 and 43 for an almost constant phase shift Δ.

The working hypothesis that the system tends to a state with minimized rate of change due to parallel current gradients, Eq. 35, and maximized radial particle flow, Eq. 34, provides a concise picture for the development of the spiraling structures triggered by resistive coupling between electron pressure and parallel electric field in the source region. These structures are triggered by the tendency to balance the pressure gradient and the parallel electric field. This determines a relation between the amplitudes of density and potential, but the phase shift is directed towards the maximum possible radial particle flow. This flow reduces the axisymmetric density and flattens its profile, i.e. the prey n_0 is eaten by the predator n_m. As a consequence the low-m mode loses its trigger, the radial gradient of n_0, and starts to diminish. This allows the axisymmetric mode n_0 to recover and the predator-prey cycle restarts again.

Parameters scans for different electron temperatures and source strength (Fig. 12) demonstrate that the simple predator-prey cycle exists in a certain parameter range only. Leaving this window leads to strong intermittencies or – contrary to that – to a quiet axisymmetric plasma column.

In a final section the relation between Eqs. 37, 43 and 41 and the predator-prey dynamics is clarified. By assuming a reasonable Gaussian profile for the axisymmetric mode n_0 Lotka-Volterra like equations for the averaged amplitudes can be derived.

The results of this work might be proven by further studies and experiments on this topic. For instance, the qualitative predictions and the basic assumptions of this work need a proof for the observed phase shift between the low-m Fourier modes n_m and ϕ_m of density and electric potential which forms a basic ingredient of the numerical plasma dynamics. Also more data are needed to confirm the assumed origin of the intermittencies in the source region, namely, parallel profiles of density and electric potential which determine the gradient lengths L_n and L_ϕ in the reduced 1D model.

However, the hypothesis that the system tends to maximize the radial flow is a conjecture similar to concepts of minimum entropy production in non-equilibrium thermodynamics [10] and can not be proven in general.

Nevertheless, this working hypothesis allows to carry on the analysis and derive a Lotka-Volterra model for the asymptotic plasma state to explain pronounced predator-prey cycles and the highly symmetric plasma state identified might serve as orientation for an assessment of operational ranges of linear machines.

Acknowledgments

This work is partially supported by NIFS/NINS under the project of Formation of International Network for Scientific Collaborations.

References

[1] H. Tanaka, N. Ohno, Y. Tsuji and S. Kajita, Contrib. Plasma Phys. **50**, 256 (2010).

[2] H. Tanaka, N. Ohno, Y. Tsuji, K. Okazaki and S. Kajita, Contrib. Plasma Phys. **52**, 424 (2012).

[3] R. Barni, C. Riccardi, Th. Pierre, G. Leclert, A. Escarguel, D. Guyomarc'h and K. Quotb, New Journal of Physics **7**, 225 (2005)

[4] M. Matsukuma, Th. Pierre, A. Escarguel, G. Leclert, D. Guyomarc'h, F. Brochard, E. Gravier, Y. Kawai, R. Redon and A. Bois, EPS Conference Proceedings, ECA Vol. 26B (ISBN 2-914771-02-9), P-5.015 (2002)

[5] K. J. Giannasi and K. J. Gibson, EPS Conference Proceedings, ECA Vol. 30I (ISBN 2-914771-40-1), P-5.162 (2006)

[6] D. Reiser, Phys. Plasmas **19**, 072317 (2012)

[7] D. Reiser and A. Mekkaoui, Fusion Science and Technology **63**, 1T, 237-240 (2013)

[8] A. Hasegawa, M. Wakatani, Phys. Rev. Lett. **50**, 682 (1983)

[9] M. Wakatani, A. Hasegawa, Phys. Fluids **27**, 611 (1984).

[10] G. Nicolis and I. Prigogine, *Self-organization in nonequilibrium systems*, (Wiley, New York, 1977)

[11] S.-D. Shih, Taiwanese Journal of Mathematics, **1**, 451 (1997)

[12] G. E. Karniadakis, M. Israeli, S. A. Orszag, Journal of Comp. Physics **97**, 414 (1991).

[13] K. U. Riemann, J. Phys. D; Appl. Phys. **24**, 493 (1991)

[14] R. H. Cohen and D. D. Ryutov, Phys. Plasmas **2**, 2011 (1995)